Measuring implosion velocities in experiments and simulations of laser-driven cylindrical implosions on the OMEGA laser

E. C. Hansen[1], D. H. Barnak[1], R. Betti[1], E. M. Campbell[1], P.-Y. Chang[2], J. R. Davies[1], V. Yu. Glebov[1], J. P. Knauer[1], J. Peebles[1], S. P. Regan[1] and A. B. Sefkow[1]

[1]Laboratory for Laser Energetics, University of Rochester, Rochester, New York 14623, USA

[2]Institute of Space and Plasma Sciences, National Cheng Kung University, Taiwan City 701, Taiwan

E-mail: ehan@lle.rochester.edu

Abstract. Laser-driven magnetized liner inertial fusion (MagLIF) on OMEGA involves cylindrical implosions, a preheat beam, and an applied magnetic field. Initial experiments excluded the preheat beam and magnetic field to better characterize the implosion. X-ray self-emission as measured by framing cameras was used to determine the shell trajectory. The 1-D code *LILAC* was used to model the central region of the implosion, and results were compared to 2-D simulations from the *HYDRA* code. Post-processing of simulation output with *SPECT3D* and *Yorick* produced synthetic x-ray images that were used to compare the simulation results with the x-ray framing camera data. Quantitative analysis shows that higher measured neutron yields correlate with higher implosion velocities. The future goal is to further analyze the x-ray images to characterize the uniformity of the implosions and apply these analysis techniques to integrated laser-driven MagLIF shots to better understand the effects of preheat and the magnetic field.

Keywords: Neutron Yields, Soft X-rays, Experiment Design, Hydrodynamics, Numerical Simulations

Submitted to: *Plasma Phys. Control. Fusion*

1. Introduction

Magnetized liner inertial fusion (MagLIF) is an alternative inertial confinement fusion (ICF) concept that involves the cylindrical implosion of preheated and magnetized fuel [1]. The purpose of the axial magnetic field is to reduce thermal conduction in the radial direction, thereby more effectively trapping heat in the center of the implosion

region. This effect has been demonstrated on spherical ICF capsules using the OMEGA laser [2, 3]. Magnetized cylindrical implosions have the potential benefit of reaching fusion-relevant conditions at lower implosion velocities and lower convergence ratios than unmagnetized spherical or cylindrical implosions.

The first MagLIF experiments were designed for and carried out on the pulsed-power Z machine at Sandia National Laboratories (SNL) [4]. Cylindrical targets were imploded via $\vec{J} \times \vec{B}$ forces by running approximately 20 MA of current through a beryllium liner. Two-dimensional magnetohydrodynamic (MHD) simulations have demonstrated that this scheme can achieve fusion-relevant conditions [4]. Initial experimental results looked promising as D_2 yields of up to 2×10^{12}, neutron-average ion temperatures of 2.5 keV, and a BR (magnetic field times radius) of approximately 0.4 T m were achieved [5], resulting in increased efforts and interest to carry out further MagLIF experiments. A laser-driven version of this platform has been developed for the OMEGA laser at the Laboratory for Laser Energetics (LLE) [6, 7]. The advantages of the laser-driven version on OMEGA include a smaller experiment to study scaling for MagLIF on future experiments, a higher shot rate to obtain more data for better statistics, and better diagnostic access for a greater variety of measurements.

The first step in this campaign was to study the cylindrical implosion without the effects of preheat and magnetic field. Cylindrical implosions have been conducted on OMEGA in the past to study magnetic flux compression [8, 9]. As compared to these earlier shots, the shots described in the present work use smaller-outer-diameter targets with varying thickness. Decreasing the shell thickness increases the implosion velocity and the yield. There is a limit, however, to how thin the shell can be: the Rayleigh–Taylor (RT) instability will become a problem if the shell is too thin [7], and RT spikes would cause a mixing issue if they penetrate the central burn region.

Experiments of direct-drive cylindrical implosions on OMEGA are complicated by the various angles of incidence. The implosion beams hit the target at varying oblique angles of $\pm 8.75°$ and $\pm 31.15°$; consequently they will refract in the coronal plasma at different depths before reaching the critical density. As the target is imploded, the on-target axial positions of the beams change. X-ray framing camera (XRFC) images were used to determine the shell trajectories. The main focus of this work is to explain how the XRFC data were used to determine the central implosion velocity.

Simulating cylindrical implosions can be challenging because the problem is inherently 3-D, but 1-D and 2-D simulations can be done with some symmetry assumptions. The 1-D *LILAC* and 2-D *HYDRA* codes were used to simulate all of the experimental shots. Post-processing of the simulation output resulted in synthetic x-ray emission images, which could then be analyzed in the same manner as the experimental images. A cohesive, quantitative analysis technique was developed to analyze both experimental and simulated x-ray self-emission images. Comparing experimental and simulation results led to important insights about the limitations of the numerical model, and the analysis technique and results can also be used to help design future experiments.

The structure of the paper is as follows: In Sec. 2, the experimental setup is

described, and the x-ray framing camera images are introduced. In Sec. 3, all of the numerical methods are described, including 1-D and 2-D simulations, generating synthetic x-ray images, and calculating the implosion velocities. The implosion velocity and neutron yield results are explained in Sec. 4. Finally, the conclusions are summarized in Sec. 5.

2. Experimental setup

A fully integrated laser-driven MagLIF shot contains several key components, as are illustrated in Fig. 1. Much of the setup is described in the point-design paper by Davies et al.[7], but a brief overview is given here for the reader.

The target is a cylinder composed of parylene-N with a typical outer diameter between 580 and 600 µm. This campaign is sometimes referred to as mini-MagLIF since the targets are about 10x smaller than MagLIF on the Z machine at SNL. The reasons for scaling down and utilizing a laser-driven platform on OMEGA have been discussed in a previous paper [6]. The cylinder is typically filled with deuterium gas to a pressure of 11 atm, which equates to approximately 1.81 mg cm^{-3} in mass density.

A single preheat beam enters the target on axis through a laser entrance hole (LEH) composed of a 1.84-µm-thick, 400-µm-diameter polyimide window. This thickness was chosen to hold up to 14 atm with a failure rate less than 50%. Other experiments have demonstrated successful preheat of up to approximately 100 eV [6]. MIFEDS (magneto-inertial fusion electrical discharge system) coils can provide an axial magnetic field of up to 10 T [10].

Studying the details of the cylindrical implosion does not require the preheat beam or the magnetic fields, so the shots relevant to the analysis in this work use only the implosion beams. There are 40 implosion beams divided into four rings. Each of the four rings contain ten beams that are aimed mostly in the radial direction (two sets of ring-3 beams and two sets of ring-4 beams). Each beam has a 1/e radius of 173.3 µm, and a peak intensity of approximately 1.7×10^{14} W/cm^2. When the target is aligned along the particular axis of choice, the ring-3 beams are incident at an angle of $\pm 31.15°$ and the ring-4 beams at an angle of $\pm 8.75°$ to normal. When all 40 beams are overlapped at these angles, the overall spot size and intensity are increased. There is some shot-to-shot variation, but the typical central on-target intensity is approximately 4.5×10^{14} W/cm^2 and the 1/e radius becomes approximately 440 µm. Altering the shell thickness and energy on target affects the implosion velocity and neutron yield for fixed laser-drive parameters, which is the main focus of this paper.

This work examines 11 different implosion-only shots, all of which used a 2-ns square pulse. Table 1 lists these shots (designated by their facility shot number) and some of the key experimental parameters. One of the main differences between shots is the cylinder thickness. Six shots were completed using a thickness of 30 µm, one shot using 24 µm, and four shots using 20 µm. Another important difference between various shots is the beam power balance, which is measured as the ratio of energy in ring 4 to

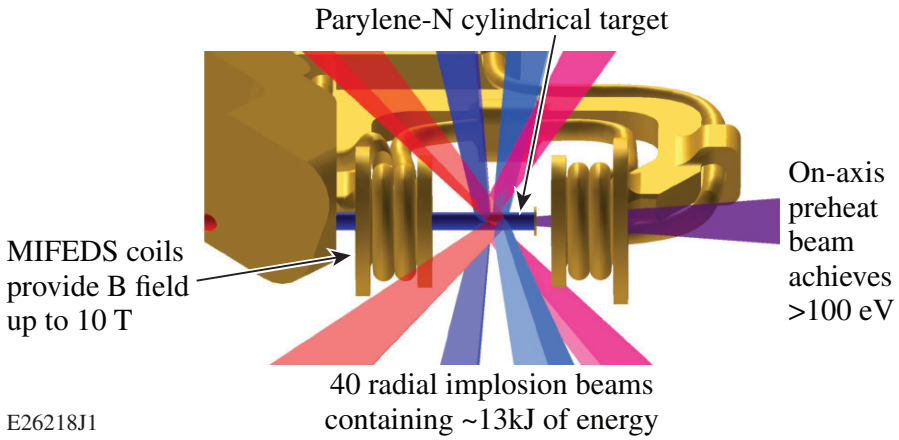

Figure 1. A schematic of the experimental setup shows the key components of a fully integrated laser-driven MagLIF (magnetized liner inertial fusion) shot. The target is cylindrical and composed of parylene-N; 40 implosion beams act in the radial direction; one preheat beam is aimed axially; and MIFEDS (magneto-inertial fusion electrical discharge system) coils produce an axial magnetic field. The shots analyzed in this work are focused on the implosion beams only; therefore the preheat beam and magnetic fields are not present.

Table 1. Experimental parameters for all implosion-only shots in this work.

Shot	Outer Diameter (µm)	Shell Thickness (µm)	E_4/E_3
79492	606.8	30	0.997
79493	578.0	30	0.996
79494	599.2	30	0.914
79495	588.4	30	0.837
79497	600.0	30	0.670
79501	601.6	30	0.807
79504	578.8	24	0.824
79498	566.0	20	0.814
79499	580.8	20	0.831
79500	592.8	20	0.811
79503	553.2	20	0.818

ring 3. Throughout this paper, shots will be referenced by their shell thickness and this beam power balance ratio E_4/E_3.

The primary diagnostics used for this experiment were x-ray framing cameras (XRFC's). Fig. 2 shows an example of the raw data from an XRFC for shot 79492. From one framing camera, 16 time frames for each shot were obtained, which were then analyzed to calculate the implosion velocity of the central region. The frames from the XRFC span the majority of the laser pulse in time and have an approximate time resolution of 50 ps per frame which is sufficient given the velocities involved. A similar analysis of shell trajectories has been carried out for spherical implosions [11, 12]. In

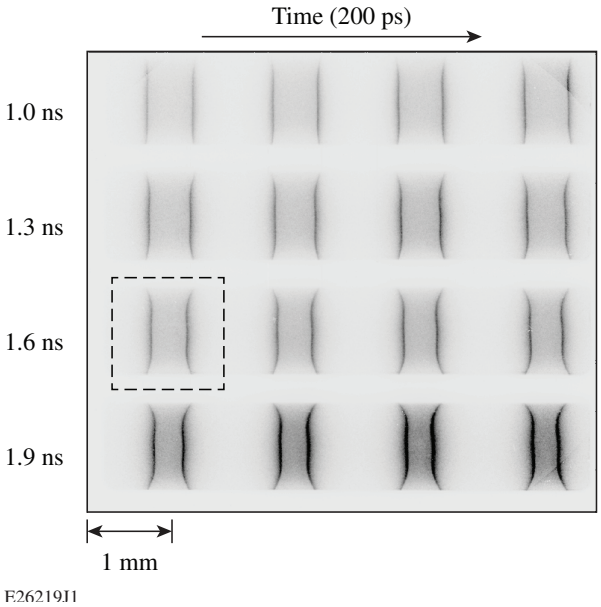

Figure 2. The raw x-ray self-emission image from shot 79492 shows the 16 time frames obtained from the XRFC. Each row starts at a requested time and represents one strip from the camera. Each strip spans 200 ps and contains four images or frames. The frame boxed in by the dashed lines is enlarged and shown in Fig. 4.

addition to the experimental images, synthetic x-ray images have been produced from simulations for comparison.

3. Numerical methods

MHD codes automatically give information about density, temperature, velocity, field strength, and many other variables. Such detailed information is not available, however, in an experiment from the various diagnostics. This is why it is useful to simulate diagnostics in order to make direct comparisons between experiment and simulation. This section describes the simulations and how the synthetic x-ray images were generated in order to compare them with experimental XRFC images.

3.1. 1-D models

LILAC is a 1-D Lagrangian hydrodynamics code that can be run in a Cartesian, cylindrical, or spherical coordinate system [13]. To model the experiment, the cylindrical geometry option was used and the radial direction was simulated. As a side note, magnetic fields have been incorporated into *LILAC*, and the new code is sometimes referred to as *LILAC-MHD-Sp* [3]. A 1-D code is limited because it can be used to model only the central region of the implosion since there is no variation in the z or ϕ directions. However, the advantage of these 1-D simulations is that they are computationally inexpensive and can be run in a matter of minutes on a single core.

The computational grid is initialized with 500 cells: 400 for the deuterium gas and

100 for the shell, which results in a maximum initial resolution of 0.2 µm for the 20-µm-thick target simulations. A laser beam is simulated with rays perpendicular to the cylindrical z axis with 2-D ray-tracing. The square pulse is simulated with a 100-ps linear ramp from zero power to full power. This eases the code into simulating the full laser power and is physically more realistic than reaching full power instantaneously via a step function.

The output is then post-processed through *SPECT3D*, a collisional-radiative spectral analysis code [14]. *SPECT3D* has many options for flexibility and can simulate different geometries, atomic models, filters, etc. The 26.4-µm-thick beryllium filter used on the XRFC to block out low-energy photons was incorporated into the model. The model also used the same resolution as the XRFC (3 µm/pixel) and included a small amount of blur through a 1-D convolution. The result is a realistic synthetic x-ray emission image of the central imploding region.

3.2. 2-D models

HYDRA is a 3-D arbitrary Lagrangian–Eulerian (ALE) MHD code [15, 16]. Like *LILAC*, *HYDRA* incorporates a variety of multi-physics, but it also includes the option of using a fully 3-D ray-tracing algorithm as well as other 2-D and 3-D physics. Simulating the cylindrical implosions in 2-D allows one to model the central imploding region more accurately. These simulations also contain important information about the axial direction, but further axially dependent analysis is beyond the scope of this paper and will be included in a separate paper.

The simulations used to model the experiment are technically 3-D, but they are considered to be 2-D simulations since they are significantly reduced in the ϕ dimension. The computational domain is a wedge that spans just 1° in the ϕ direction with one computational cell. Therefore, the simulations are effectively 2-D in r and z. Fig. 3 is a *VISRAD* [17] drawing of the simulated domain and the different regions in the $r - z$ plane. Note that a 2-D simulation allows for the use of the measured beam pointing and power balance from the experiment.

The computational grid is composed of 135 by 200 computational cells for the r and z dimensions, respectively. In the r direction, there are 60 cells for the gas, 60 cells for the shell, and 15 cells for the vacuum. The z direction spans 2 mm, and the upper-r boundary is set far enough away from the shell to avoid any potential boundary issues from ablated material. The mesh is feathered to achieve a maximum resolution of 0.1 µm near the cylinder edges. *HYDRA* is a parallelized code, so these simulations are run on 16 cores to reduce computational time.

Post-processing the simulation output with *SPECT3D* became cumbersome in this particular geometry, so an alternative method was used. A post-processing *Yorick* routine was developed to produce 2-D synthetic x-ray emission images from *HYDRA* output. Since *HYDRA* is a radiative hydrodynamics code, it has the necessary emissivities and opacities for this calculation. *Yorick* is an interpreted language

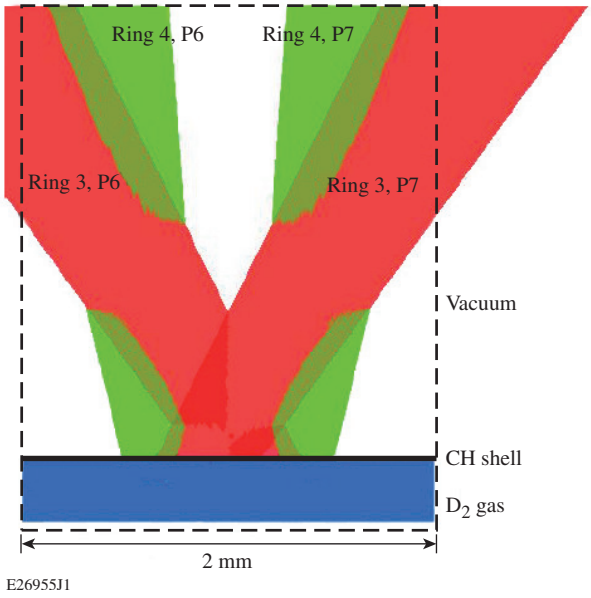

Figure 3. A *VISRAD* drawing shows the simulated vacuum (white), gas (blue), and shell (black) regions, as well as an accurate representation of the beams. The left and right sides of the domain are denoted by the port numbers of the OMEGA target chamber (P6 and P7). The boxed-in region represents the computational domain. Due to the positions and angles of the rings, the ring-3 beams (red) drive the center of the implosion, while the ring-4 beams (green) drive the outer regions of the implosion.

commonly used as a pre-processor or post-processor for physics simulation codes [18]. Examples of synthetic x-ray images produced with *HYDRA* and *Yorick* will be shown later in this paper.

3.3. Calculating implosion velocities

The main results contained in this work come from a quantitative analysis of the experimental XRFC images and the simulated x-ray images. A lineout is taken through the center of an x-ray image (shown in Fig. 4) in order to calculate an implosion velocity. The lineout is an average of the data over a dz = 60-µm-long region to reduce noise. Data from the lineout are then fitted with a 7-Gaussian function. Fig. 4 shows how well this type of fit works for data from the 30-µm-thick, $E_4/E_3 = 0.997$ shot. Multiple Gaussians are needed because the implosion is not perfectly symmetric. Reasons for this include, but are not limited to, target quality, imperfect beam balance, and camera tilt or skew. Furthermore, the emission from either side (right or left) of the cylinder is itself not symmetric, because the inner region of imploding gas is hotter than the outer vacuum region.

For a given shot, the 7-Gaussian fits are computed for the 16 time frames obtained from the XRFC (see Fig. 2). Then, from these fits, the distances of the peak-to-peak emission are calculated. The positions used to calculate velocities are these peak-to-peak distances (divided by two), which helps account for the aforementioned asymmetries.

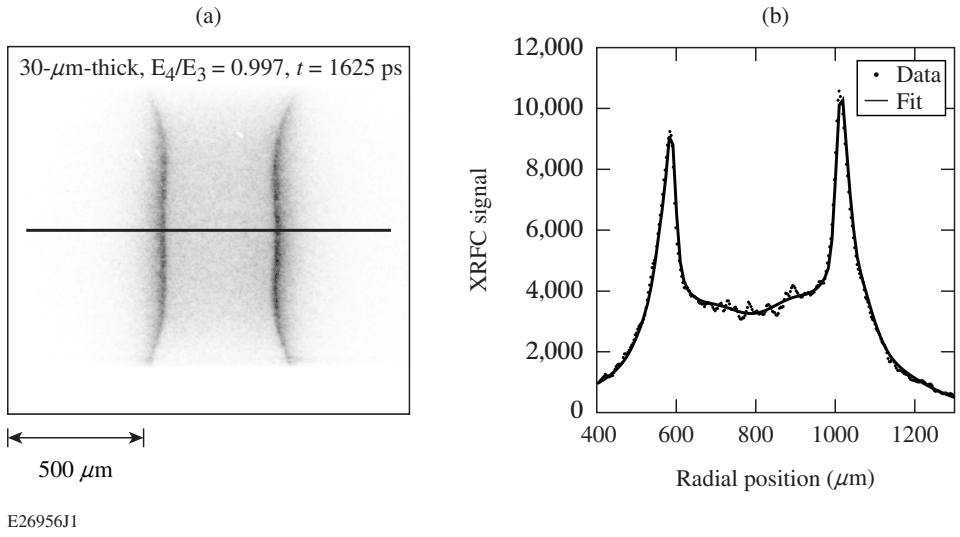

Figure 4. (a) An enlargement of the ninth frame from the XRFC image from shot 79492 previously shown in Fig. 2. The horizontal line shows where a lineout is taken as the first step towards calculating the implosion velocity. (b) The data from the lineout is shown alongside the 7-Gaussian fit used to find the positions of the peaks of the emission.

Fig. 5 shows these positions versus time for three shots from experimental data. Each of the three shots shown has a different shell thickness of 30, 24, or 20 µm. The implosion velocity is then calculated as the slope of a best-fit line to the position versus time data. Although there is a relatively short acceleration phase early in time (before the XRFC images), the implosion velocity is approximately constant during the XRFC acquisition, thus the straight-line fits are an appropriate means of comparing simulations and experiments. Fig. 5 also shows these best-fit lines, and it is observed that thinner shells lead to higher implosion velocities. This makes intuitive sense because a thinner shell would have less inertia than a thicker shell, making it easier to implode. Note that the 20 µm-thick shot shows evidence of acceleration at late times. The 24 µm-thick and 30 µm-thick shots may also show acceleration at even later times, but velocities are calculated during the same time (the laser pulse) for a consistent shot-to-shot comparison.

The implosion velocities calculated in this work are calculated from the positions of the peak x-ray emission which is not the typical definition of implosion velocity. A more traditional definition would track the position of the fuel-shell interface over time [7]. To avoid confusion, the implosion velocity calculated via the fuel-shell interface will be called the "fuel" implosion velocity, and the implosion velocity calculated via x-ray emission will be called the "x-ray" implosion velocity. The two types of implosion velocities are related, and this can be seen in Fig. 6. In these simulations, the fuel implosion velocity is always higher than the x-ray implosion velocity, and they are approximately proportional ($v_{fuel} \approx 0.80 v_{x-ray} + 48.38$). The main advantage of using the x-ray implosion velocity is that it can be calculated from simulations and

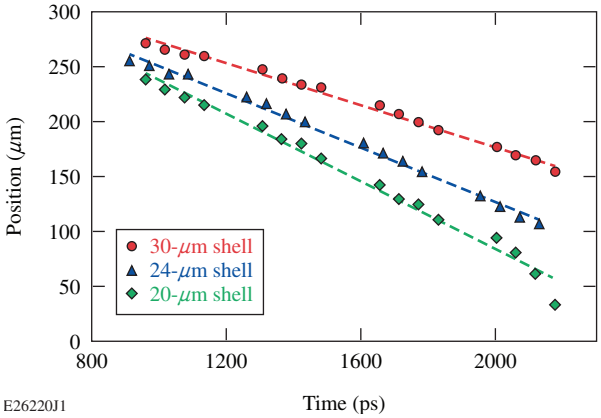

Figure 5. Peak positions of the emission, as calculated from the XRFC lineout fits, are shown for three different shots with different shell thicknesses. They are plotted versus time; the dashed lines represent the best-fit lines to this data. Implosion velocities are calculated from the slopes of these best-fit lines, and it is immediately observed that thinner shells lead to higher implosion velocities.

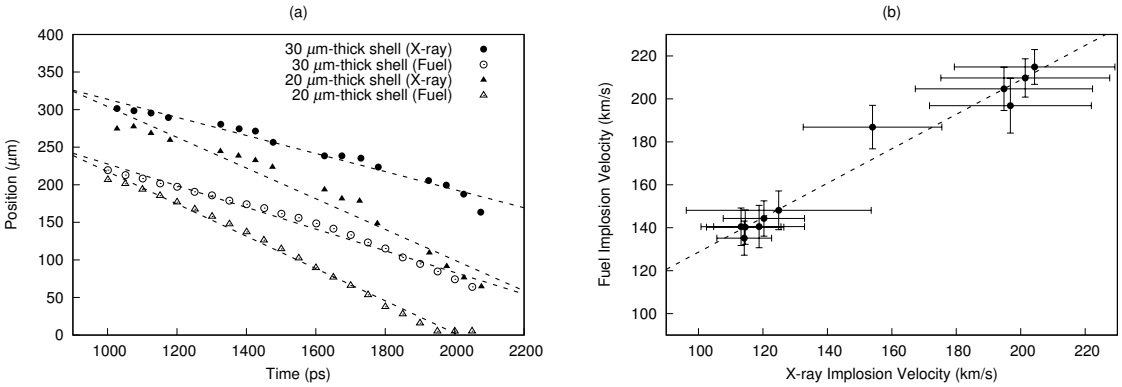

Figure 6. (a) Position versus time data from simulations of a 20 µm-thick shell and a 30 µm-thick shell. The plot shows both the positions of peak x-ray emission and the outer fuel radius. Best-fit lines show that the implosion velocities measured via outer fuel radii follow the same trend as the "x-ray" implosion velocities. (b) Fuel implosion velocity versus x-ray implosion velocity for all simulations. The dashed line is a best-fit line which shows that the two velocities are approximately proportional.

experiments using the same method; this makes for a more accurate simulation-to-experiment comparison. For the remainder of this work, all implosion velocities refer to the x-ray implosion velocity as previously described.

4. Results

4.1. 1-D simulations

The OMEGA laser is normally configured to implode spherical targets using 60 beams arranged symmetrically. Since mini-MagLIF targets are cylindrical, the beams will have

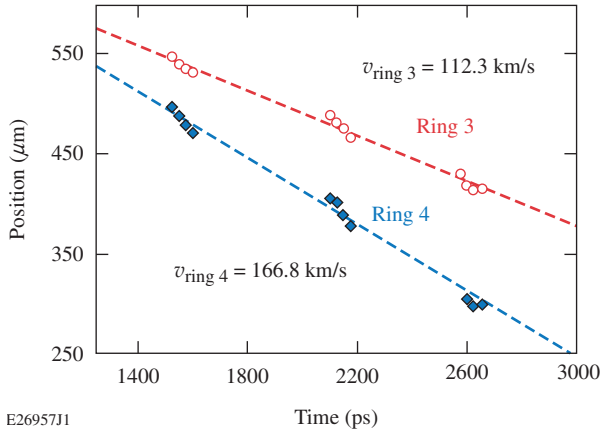

Figure 7. Trajectories of shells using either rings 3 or rings 4 to drive the implosion. The difference in laser absorption between the two incidence angles is highlighted by the difference in shell velocities from the linear fitting of the trajectory points.

different axial locations and unique angles of incidence (±31.15° for rings 3 and ±8.75° for rings 4). Thus, initial shots were performed to understand the drive from rings 3 and rings 4 individually. Empty cylinders composed of CH plastic were imploded with two overlapped rings, either the two rings 3 or the two rings 4. Both cases used the same laser power with a 2.5-ns square pulse.

The x-ray images were analyzed as described in the previous section, and implosion velocities were calculated. Fig. 7 shows the resulting velocities for the ring-3 and ring-4 cases. The velocity related to the ring-4 beams is higher because the laser absorption is more efficient at the smaller angle of incidence θ.

One-dimensional simulations using *LILAC* were then conducted to match the velocities calculated from experiment. *LILAC* requires laser power per unit length as input; therefore this must first be calculated at the center of the imploding cylinder from experimental parameters. For a given energy, the intensity on the surface of the cylinder can be written as

$$I(z)_i = I_{o,i}\left[\mathrm{e}^{-(z-d_i)^2/r_i^2} + \mathrm{e}^{-(z+d_i)^2/r_i^2}\right], \tag{1}$$

where z is the position ($z = 0$ is the center), d_i is axial displacement, and r_i is the beam width. The index i denotes the ring number; values differ between rings 3 and 4 on OMEGA. The displacement d_i is more generally written as

$$d_i = \tan(\theta_i)R + s_i, \tag{2}$$

where θ_i is the angle of incidence (0° is normal to the target surface), R is the target outer radius, and s_i is an on-axis offset. Table 2 lists the beam-pointing parameters for rings 3 and 4 for the gas-filled shots. The empty-cylinder, single-ring shots differ only in that the displacements s_i were smaller in order to achieve a flat intensity profile.

The total energy on target E can be written as an integral of the intensity $I(z)$

Table 2. Experimental beam pointing parameters for rings 3 and 4.

	r (µm)	θ (deg)	s (µm)
Ring 3	202.5	31.15	-280
Ring 4	175.3	8.75	275

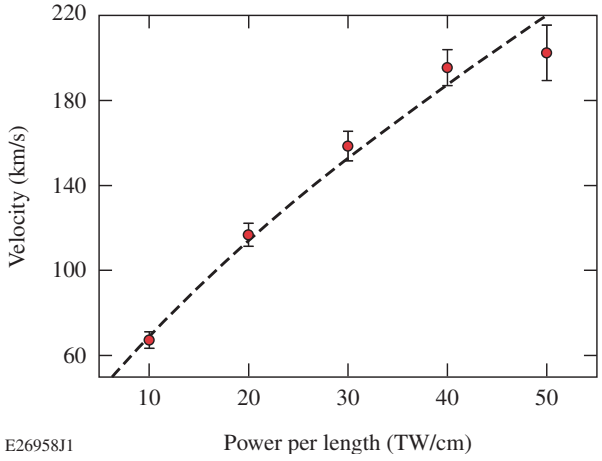

Figure 8. The simulated implosion velocity from 1-D *LILAC* simulations is affected by the input laser power per length. From the power-law fit, it is determined that the input power must be reduced to 49% for ring 3 and 89% for ring 4 in order for the simulated implosion velocity to match the experimental implosion velocity. The power reduction is necessary because *LILAC* does not account for the angle of incidence of the beams.

over space and time:

$$E = \int \int I(z) 2\pi R \, \mathrm{d}z \, \mathrm{d}t. \tag{3}$$

The peak intensity I_o can be found by combining this integral with Eq. (1). Solving for the power per unit length at the center of the target results in the following equation:

$$P_L = I(0) 2\pi R. \tag{4}$$

Using this power per length as input in *LILAC* ultimately results in an implosion velocity that is much too high compared to experiments. A systematic approach was employed to determine what the input power per length should be. Five different simulations varying only the input power per length were run. Next, the implosion velocity was calculated for each simulation from synthetic x-ray images. Fig. 8 shows the velocity versus power data for these five simulations and a power law that fits the data. The derived power law is

$$v = 13.563 P_L^{0.7107}, \tag{5}$$

where P_L is in TW cm^{-1} and v is the velocity in km s^{-1}.

The power law helps one to determine what power per length to use in *LILAC* to match the implosion velocity calculated from experiment. It is necessary to use 49% of

the experimental power per length to achieve the correct velocity in the ring-3 case. For the ring 4-case, the simulation required 89% of the experimental power per length. The reduction in power required by the simulation corresponds to the reduction in drive due to the differing angles of incidence and other factors. These percentages are lower than expected from theory using the $\cos^2\theta$ law because the azimuthal angle of incidence is also not accounted for. Furthermore, it is likely that cross-beam energy transfer (CBET) [19] removes some energy from the beams, especially at later times during the implosion.

By taking into account the laser-absorption efficiency for each ring, one can choose an appropriate beam pointing for shots that use both rings. The results from the single-ring shots and simulations revealed that the on-target intensity from ring 4 is almost twice that of ring 3 ($I_{o,4} \approx 1.82 I_{o,3}$). Using this information, it was determined that spreading the rings apart with displacements s_i (listed in Table 2) results in a relatively flat intensity profile.

For the *LILAC* simulations that incorporated energy from both rings for the gas-filled shots, the input power per length had to be reduced by about 50% in order to match the experimental implosion velocity. This is not surprising and is consistent with the results from the single-ring experiments because the center of the implosion is primarily driven by ring 3 (ring 4 does not deposit much energy at the center).

4.2. 2-D simulations

Fig. 9 shows an example of a synthetic x-ray image from a 2-D *HYDRA* simulation of shot 79494 alongside the position measurements. This figure also shows the corresponding position measurements from experiment. Notice that the slopes of the best-fit lines (i.e., the velocities) are approximately equal, but there is an apparent offset of about 250 ps. There are several possible explanations for why the simulated positions are always larger than the experimental positions. Discrepancies in the requested XRFC timings and the actual XRFC timings have been observed, and if the XRFC measurements are simply shifted later in time, the experimental and simulated data line up. There are also many factors on the simulation side, such as emissivity, opacity, equation of state, thermal conductivity, flux limiters, etc., that can introduce a systematic offset. Investigating this further is beyond the scope of this paper since matching the velocity was the primary goal.

A comparison of simulated velocity measurements with the experimental values from XRFC data shows that the two are consistent (see Fig. 10) for all shots. The simulations typically show implosion velocities that are higher than the experimental values, but they are still within the error bars. Note also in Fig. 10 that there is a natural grouping of velocities by shell thickness: all 30-µm-thick shots are at the low end of velocity, all 20-µm-thick shots are at the high end, and the one 24-µm-thick shot is in between. Unlike the 1-D *LILAC* simulations, there was no need to alter the input laser power to match the experimental implosion velocities. Because of the ability to use the correct angles of incidence for the beams and to simulate the axial direction, the

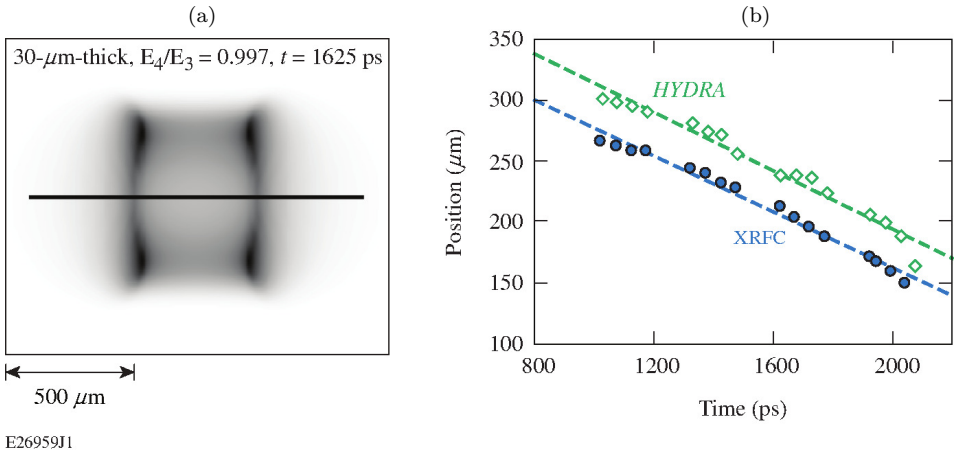

Figure 9. (a) An enlargement of a simulated x-ray image from shot 79494 with the overlaid horizontal lineout. (b) The position versus time measurements for shot 79494 from simulation and experiment. Note that the slopes (i.e., velocities) are approximately equal, but there is an apparent offset in time.

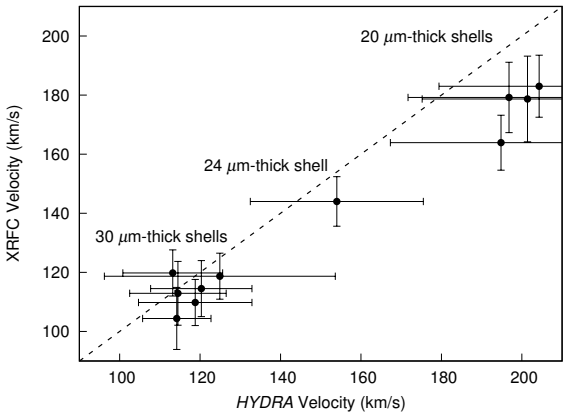

Figure 10. Experimental and simulated (determined by the fitting routine) x-ray implosion velocities are displayed in this plot with error bars to show that they were consistent. The dashed line has a slope of 1.0. The experimental velocities were calculated from the XRFC data, and the simulated velocities were calculated from *HYDRA* simulations using the same analysis technique. The error bars are from the fitting procedure (i.e., errors in the slopes of the best-fit lines).

2-D simulations were able to provide an accurate model of the center of the implosion.

4.3. Neutron yields

A neutron time-of-flight (nTOF) detector was used to measure deuterium–deuterium neutron yields for each shot. The measurements are listed in Table 3 alongside the implosion velocities calculated from the analysis described in Sec. 3.3. The measured neutron yields were not high enough to obtain reliable neutron-averaged ion temperatures, but future shots will use a new re-entrant nTOF detector that will allow for temperature measurements at lower yields.

Table 3. Implosion velocities and measured neutron yields for all shots.

Shot	Velocity ($\mathrm{km\,s^{-1}}$)	Yield (10^6)
79492	109.8	0.46
79493	118.7	2.92
79494	114.5	5.86
79495	112.9	4.45
79497	104.4	1.31
79501	119.8	3.67
79504	144.0	9.79
79498	163.9	25.30
79499	178.7	62.40
79500	183.0	74.90
79503	179.2	15.90

The implosion velocity correlates very well with the measured neutron yield. Fig. 10 showed that the velocities naturally grouped together by shell thickness, so the velocities and neutron yields were averaged by shell thickness. The weighted averages are plotted in Fig. 11, where the trend convincingly shows that higher implosion velocities lead to higher neutron yields. A power-law fit, also shown in the figure, is represented by the equation

$$Y = 3.2 \times 10^{-20} v^{9.3738}, \tag{6}$$

where Y is the yield in 10^6 neutrons and v is the velocity in $\mathrm{km\,s^{-1}}$. The power-law is calculated from a weighted fit to account for larger errors in the single 24 µm data point. This is not a surprising result, but it is a verification that cylindrical implosions behave as expected. Furthermore, it shows that a shell thickness of 20 µm leads to higher yields with no apparent issues relating to mix or RT instabilities. Measuring emission from implosions of doped shells would be one way to characterize the potential influence of mix or RT instabilities, but this is beyond the scope of this work. All future shots including preheat and magnetic fields will use targets with a 20-µm shell thickness.

Although the nTOF detectors were unable to reliably measure neutron bang times or ion temperatures, some fusion-relevant information can be obtained from the simulations. Table 4 lists the results of several calculations from three different simulations: neutron bang times, central convergence ratios, neutron-averaged densities at bang time $< \rho >$, and neutron-averaged ion temperatures at bang time $< T_i >$. The convergence ratio is calculated at the center of the implosion region, so it may be higher or lower at different axial positions depending on drive uniformity. Future shots will be most similar to shot 79500, but still different enough that these calculations will lead to different results. Calculating these fusion-relevant quantities will be an important part of comparing future shots to the larger MagLIF experiments on Z.

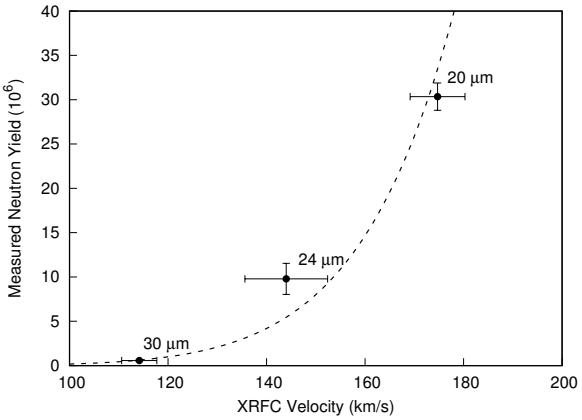

Figure 11. A higher implosion velocity leads to a higher measured neutron yield. The results in this plot are averaged by shell thickness. The dashed line represents a weighted power-law fit. The error bars on the neutron yields are a combination of statistical error, based on the number of neutrons entering the detector, and standard error in the measurements being averaged.

Table 4. Bang times, convergence ratios, neutron-averaged densities, and neutron-averaged ion temperatures from simulations of shots 79492, 79504, and 79500.

Shot	Bang time (ns)	Convergence ratio	$< \rho >$ (g/cm^3)	$< T_i >$ (keV)
79492	2.38	53.7	11.2	1.10
79504	2.10	53.2	10.5	1.17
79500	1.95	41.1	6.43	1.37

5. Summary and conclusions

Understanding cylindrical implosions was the first step in the laser-driven MagLIF campaign on OMEGA. To investigate these implosion-only shots, x-ray self-emission images were recorded without a preheat beam or applied magnetic field. A quantitative analysis was developed to measure implosion velocities from both experimental and simulated x-ray images.

Before gas-filled shots were conducted, rings 3 and rings 4 were tested individually to better understand the effect of beam obliquity. The differences in measured implosion velocities were due to the target's absorption of energy from rings 3 versus rings 4. One-dimensional (1-D) *LILAC* simulations helped determine that rings 3 and rings 4 had an absorption efficiency of approximately 49% and 89%, respectively. This information led to the beam pointing used for the first gas-filled shots.

On those subsequent gas-filled shots, the role of shell thickness was investigated. The same analysis of experimental and simulated x-ray images was employed, and it showed conclusively that thinner shells led to higher implosion velocities and higher yields. Furthermore, since there was no evidence that the RT instability hindered the

yield, a shell thickness of 20 µm was chosen for future shots.

Two-dimensional (2-D) *HYDRA* simulations of the experiment including measured beam pointings and 3-D ray-tracing were performed. These simulations were able to provide an accurate model of the center of the implosion without any alteration to the input power, whereas the input power in 1-D *LILAC* simulations had to be reduced by about a factor of 2. This confirms that the angle of incidence is the primary reason for the loss of drive, which is not accounted for in *LILAC*. The azimuthal angle of incidence and CBET are also likely contributors to the loss of drive, and they are not accounted for in either *LILAC* or the 2-D *HYDRA* simulations. Further investigation is needed to determine the significance of these effects.

Much effort was spent in developing the quantitative analysis method and in generating synthetic x-ray emission images. It is essential that these methods be used for future investigations of laser-driven MagLIF experiments and simulations. A complimentary paper on the implosion-only shots for this campaign will investigate the shape of the x-ray emission. This will help to determine drive uniformity and will aid in optimizing the beam pointing and beam power balance. In the near future, these analysis techniques will be applied to fully integrated laser-driven MagLIF shots that will include preheat and magnetic fields. Preheat and magnetic fields may have significant impacts on core emission, which can also be observed via XRFC images.

Acknowledgements

The information, data, and work presented herein was funded in part by the Advanced Research Projects Agency-Energy (ARPA-E), the U.S. Department of Energy, under Award No. DE-AR0000568, the Department of Energy National Nuclear Security Administration, under Award No. DE-NA0001944, the University of Rochester, and the New York State Research and Development Authority. The views and opinions of authors herein do not necessarily state or reflect those of the United States Government or any agency thereof.

References

[1] Slutz S A, Hermann M C, Vesey R A, Sefkow A B, Sinars D B, Rovang D C, Peterson K J and Cuneo M E 2010 *Phys. Plasmas* **17** 056303
[2] Chang P Y, Fiksel G, Hohenberger M, Knauer J P, Betti R, Marshall F J, Meyerhofer D D, Séguin F H and Petrasso R D 2011 *Phys. Rev. Lett.* **107** 035006
[3] Hohenberger M, Chang P Y, Fiksel G, Knauer J P, Betti R, Marshall F J, Meyerhofer D D, Séguin F H and Petrasso R D 2012 *Phys. Plasmas* **19** 056306
[4] Sefkow A B, Slutz S A, Koning J M, Marinak M M, Peterson K J, Sinars D B and Vesey R A 2014 *Phys. Plasmas* **21** 072711
[5] Gomez M R *et al.* 2014 *Phys. Rev. Lett.* **113** 155003
[6] Barnak D H *et al.* 2017 *Phys. Plasmas* **24** 056310
[7] Davies J R, Barnak D H, Betti R, Campbell E M, Chang P Y, Sefkow A B, Peterson K J, Sinars D B and Weis M R 2017 *Phys. Plasmas* **24** 062701
[8] Gotchev O V *et al.* 2009 *Phys. Rev. Lett.* **103** 215004

[9] Knauer J P *et al.* 2010 *Phys. Plasmas* **17** 056318
[10] Fiksel G *et al.* 2015 *Rev. Sci. Instrum.* **86** 016105
[11] Michel D T, Sorce C, Epstein R, Whiting N, Igumenshchev I V, Jungquist R and Froula D H 2012 *Rev. Sci. Instrum.* **83** 10E530
[12] Michel D T *et al.* 2015 *High Power Laser Sci. Eng.* **3** e19
[13] Delettrez J and Goldman E B 1976 Rochester, NY: Laboratory for Laser Energetics, University of Rochester LLE Report No. 36
[14] MacFarlane J J, Golovkin I E, Wang P, Woodruff P R and Pereyra N A 2007 *High Energy Density Phys.* **3** 181
[15] Marinak M M, Tipton R E, Landen O L, Murphy T J, Amendt P, Haan S W, Hatchett S P, Keane C J, McEachern R and Wallace R 1996 *Phys. Plasmas* **3** 2070
[16] Marinak M M, Kerbel G D, Gentile N A, Jones O, Munro D, Pollaine S, Dittrich T R and Haan S W 2001 *Phys.Plasmas* **8** 2275
[17] MacFarlane J J 2003 *J. Quant. Spectrosc. Radiat. Transf.* **81** 287
[18] Munro D 1995 *Comput. Phys.* **9** 609
[19] Myatt J F, Follett R K, Shaw J G, Edgell D H, Froula D H, Igumenshchev I V and Goncharov V N 2017 *Phys. Plasmas* **24** 056308